Advanced Materials

ADVANCED MATERIALS
www.advmat.de

RESEARCH ARTICLE

Modular Opto-Magnetic Oscillators: Harnessing Light to Drive Versatile Materials and Functionalities

Ying-Hao Fu[1] | Meng Li[2] | Aniket Pal[3] | Zi-Ting Wang[1] | Tao Wang[1] | Yu Wang[1] | Wen Qiao[4] | Xiaoshi Qian[5] | Yan-Qing Lu[1]

[1]National Laboratory of Solid-State Microstructures, Key Laboratory of Intelligent Optical Sensing and Manipulation, College of Engineering and Applied Sciences, and Collaborative Innovation Center of Advanced Microstructures, Nanjing University, Nanjing, China | [2]Laboratory For Advanced Biopolymers, Department of Civil and Environmental Engineering, Massachusetts Institute of Technology, Cambridge, Massachusetts, USA | [3]Institute of Applied Mechanics, University of Stuttgart, Stuttgart, Germany | [4]School of Optoelectronic Science and Engineering and Collaborative Innovation Center of Suzhou Nano Science and Technology, Soochow University, Suzhou, China | [5]State Key Laboratory of Mechanical System and Vibration, MOE Key Laboratory for Power Machinery and Engineering, and Interdisciplinary Research Center, School of Mechanical Engineering, Shanghai Jiao Tong University, Shanghai, China

Correspondence: Yu Wang (yuwang87@nju.edu.cn) | Wen Qiao (wqiao@suda.edu.cn) | Yan-Qing Lu (yqlu@nju.edu.cn)

Received: 15 October 2025 | **Revised:** 14 January 2026 | **Accepted:** 4 February 2026

Keywords: modular assembly | multi-technology interface | opto-magnetic feedback | self-sustained oscillation | soft robotics

ABSTRACT

Self-sustained oscillations are fundamental to dynamic systems in nature, such as heartbeats, ocean waves, and firefly flashes. However, creating similar autonomous, out-of-equilibrium behaviors across diverse materials and structures in artificial settings remains challenging due to the lack of a universal, platform-independent control method. Here, we present an opto-magnetic feedback control strategy that achieves reliable self-excited oscillations through combined light, magnetic, and mechanical interactions based on a modular design approach. The dynamic, plug-and-play assembly of driving and deforming modules endows the platform with exceptional versatility in material type, structural setup, mechanical response, and functional use. Notably, this system can be tuned to produce continuous or intermittent self-oscillations, demonstrating its adaptability. We showcase the broad utility of the system by integrating optical modules for reconfigurable dynamic displays and wide-field-of-view light scanning, together with a thermo-mechano-electrical transduction module for high-efficiency energy harvesting. The proposed approach establishes a universal feedback pathway linking autonomous soft machines with various technological platforms, enabling on-demand adaptation across different application scenarios.

1 | Introduction

Biological systems have evolved to move in response to their surrounding environment, whether to prey/forage, evade predators, or adapt to natural disasters, all in the interest of survival. The diverse responsiveness of biological systems to environmental stimuli has inspired the development of soft, smart actuating materials that mimic their behaviors. However, many current artificial soft actuators generate either single, transient motion under short-duration stimuli [1, 2] or periodic, continuous motion in response to modulated stimuli [3–5]. While effective in some contexts, they fail to exhibit the autonomous, adaptive, and intelligent responsiveness seen in natural organisms. To address this gap, autonomous actuating systems, particularly self-sustained oscillations, have garnered significant interest for their ability to generate continuous, energy-efficient, and interactive motions

---

Ying-Hao Fu and Meng Li contributed equally to this work.

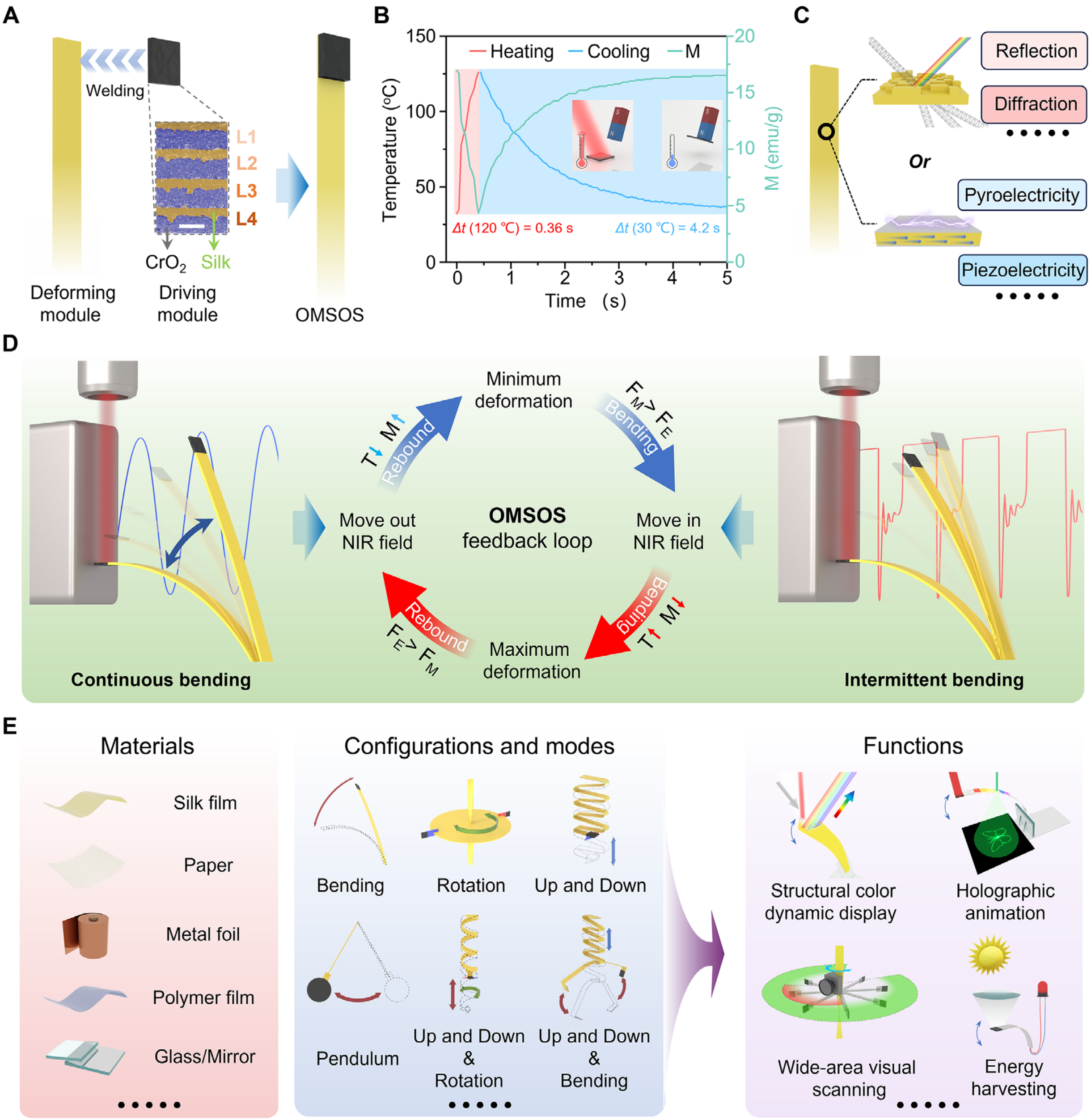

FIGURE 1 | Design, mechanism, and versatility of OMSOS. (A) The modular design of the OMSOS, which consists of a driving module and a deforming module. The inset shows the SEM image of the cross-section of the driving module consisting of 4 layers of CrO_2@SF film welded together. Scale bar: 50 µm. (B) Dependence of temperature and magnetization of the driving module on the near-infrared (NIR) laser illumination time ($I = 150$ mW/mm^2). The driving module exhibits temperature-dependent magnetic modulation, where heating reduces magnetization while cooling restores it. The magnetic driving module is heated to 120°C in 0.36 s ($I = 150$ mW/mm^2) and cooled down to 30°C in 4.2 s. Insets indicate thermally induced demagnetization. (C) The versatile design options of the deforming module, including customizable surface topographies and varied material properties. (D) The self-oscillating negative feedback mechanism of OMSOS using unmodulated light and magnetic fields. (E) The versatility of the OMSOS, featuring broad materials compatibility, multi-configuration and multi-modal operation, and programmable functionalities.

using unmodulated external stimuli, resembling the dynamic behaviors of living systems [6, 7]. They operate through built-in feedback loops connecting material properties, mechanical deformation, and external stimuli, enabling motion that continuously transforms between two or more metastable states under constant energy sources and controls. Moreover, the reduced requirement using unmodulated stimuli allows these systems to harness ubiquitous natural energy sources such as sunlight [8, 9], thermal energy [10, 11], water vapor [12], fluid flow [13], and moisture [14]. Utilizing these capabilities, self-oscillating material systems have been applied in soft robotics [15], material transport [16], bio-mimetic systems [17], energy conversion [18–20], sensing [21], and photonic modulation [22, 23].

Following the conceptual framework, achieving self-oscillating actuation hinges on strategies that effectively initiate and sustain the out-of-equilibrium states within the system. To date, self-oscillating motions have been studied in non-equilibrium material systems based on mechanisms including Belousov–Zhabotinsky reaction [24–26], self-shadowing effect [8, 9, 15, 17, 18, 23, 27–32], gradient stimulus field [14, 19, 20, 22, 33–35], and phase transition [36]. Leveraging these principles, Self-oscillating systems have made remarkable advancements in material innovation [37, 38], high-performance oscillation [9, 17], diverse motion modes [23, 28], and interfacing with other technologies [16, 20, 23]. However, despite great success in autonomous oscillatory motions, a persistent challenge remains: existing implementations predominantly rely on specialized, actively responsive materials to construct the majority, if not all, of the deforming components of self-oscillating devices. This reliance on tailored, irreplaceable materials dramatically restricts the flexibility in material selection, configuration, deformation modes, and integrated functionalities, as well as the adaptivity to diverse environments or tasks, thereby hindering the universality and versatility of the self-oscillating systems. Therefore, a novel self-oscillating strategy is desirable to break free from material-specific constraints, enabling more adaptable, scalable, and multifunctional solutions for various practical applications.

Here, we present a wirelessly controlled, modular self-oscillating system powered by unmodulated light and magnetic fields. We propose that the optically induced demagnetization strategy offers an exceptional opportunity for a plug-and-play paradigm for assembling the driving and deforming modules, in stark contrast to conventional monolithic approaches, endowing the self-oscillating system with unprecedented flexibility in composition, configuration, oscillation mode, and functionality. We demonstrate that this system can be tuned to exhibit either continuous or intermittent multi-modal self-oscillations with controllable amplitude and frequency. Leveraging these capabilities, we showcase applications including dynamic optical display using surface-patterned silk fibroin (SF) cantilevers, light scanning via aluminum reflectors, and electrical energy harvesting with polyvinylidene fluoride (PVDF) cantilevers.

2 | Result

2.1 | Modular Design and Self-Oscillation Mechanism

The opto-magnetic self-oscillating system (OMSOS) comprises a driving module and a deforming module. Figure 1A illustrates a typical modular assembly configuration designed to generate bending oscillations, consisting of an elastic cantilever serving as the deforming module and a patch of 4-layered composite films of chromium dioxide and silk fibroin (CrO_2@SF) laminated at one end as the driving module. The driving module—the CrO_2@SF patch—generates an active magnetic force in response to an external magnetic field. Crucially, this active force can be precisely modulated via light irradiation due to the high photothermal conversion efficiency and low Curie temperature of CrO_2 [39]. These properties enable photo-induced demagnetization (Figure 1B), thus allowing for a dynamic and non-contact control over the magnetic actuation. The deforming module, which can consist of diverse materials, is designed to mechanically counterbalance the magnetic force through a passive force (e.g., elasticity or gravity) while simultaneously providing application-specific functionalities by strategically tailoring its surface topography or material properties (Figure 1C).

The OMSOS system achieves self-sustained oscillation through a unique negative feedback loop mechanism that dynamically balances temperature- and position-dependent magnetic forces with motion-induced passive forces under the synergistic stimulation of light and magnetic fields (Figure 1D, Movie S1). In contrast to conventional oscillators, which are limited to continuous motion, our system exhibits dual-mode operation, supporting both continuous and intermittent self-oscillations. In the continuous mode (Movie S2), the motion follows a smooth, uninterrupted trajectory with consistent reciprocating behavior, maintaining perfect periodicity through sequential "deformation-release" cycles. In contrast, intermittent self-oscillation is characterized by distinct pauses at both trajectory endpoints, asymmetric reciprocating paths, and elastic jitter during rebound (Movie S2). As a result, the intermittent self-oscillation follows a more complex cycle of "deformation-pause-release-jitter". This distinctive capability arises from the system's unique capacity to independently modulate the active magnetic force (F_M) and passive elastic forces (F_E). When these two forces are precisely balanced, even a small temperature-induced change in magnetic force is sufficient to reverse the direction of the net force, enabling continuous self-oscillations. However, under deliberate force mismatch ($F_M \gg F_E$), the system requires an extended heating period to sufficiently weaken magnetic dominance for motion reversal, resulting in characteristic intermittent oscillations.

As the core actuating component in the OMSOS, the driving module leverages its superior photothermal conversion and thermal demagnetization properties to tune the magnetic force rapidly (Figure 1B; Figure S1), which is crucial for achieving a high self-oscillating performance throughout the system. Additionally, the driving module demonstrates mechanical robustness, morphing flexibility, strong interfacial adhesion and weldability, and thermal stability, thereby ensuring structural integrity, programmable deformation, seamless integration with the deforming module, and reliable operation. These attributes are supported through an SF-based composite architecture, where the SF matrix serves as a versatile host for CrO_2 particle doping while maintaining its intrinsic magnetic performance. The CrO_2@SF film is mechanically robust and flexible (Figure S2); it can be readily transformed into diverse 3D configurations using water-vapor-assisted origami and kirigami techniques [40] (Figure S3). The CrO_2 particles are uniformly distributed in-plane but aggregate at the bottom of the film (Figure S4) due to particle settling during the drying process. Leveraging the strong adhesion properties of the amorphous SF matrix [40], this naturally occurring separation is favorable in stacking multiple CrO_2@SF films together (Inset in Figure 1A) and interfacing with other substrates (Figure S5). When bonded with another SF surface, the interface is invisible and inseparable, demonstrating strong adhesion and seamless welding that ensures efficient photothermal conversion and magnetic coupling. Furthermore, the driving module demonstrates excellent stability of its chemical structure and reversibility of its magnetic properties under long-term thermal cycling (Figure S6), enhancing the overall reliability of the self-oscillating system.

The self-sustained oscillation in this work has collective advantages over other self-oscillating systems, as summarized in

Table S1. The modular design, which separates the driving module from the deforming module, enhances the system's versatility in terms of material selection, configuration, oscillation mode, and functional design. The body material can be readily functionalized or substituted to accommodate diverse performance demands and functional requirements. By strategically engineering the assembly configuration of driving and deforming modules, multi-modal oscillation, such as bending, rotation, linear translation, pendulum, and a combination of these modalities, can be achieved. These flexibilities make the self-oscillating system highly adaptable to various application scenarios, including structural color dynamic displays, holographic animation, optical scanning, and energy harvesting. These favorable features are illustrated in Figure 1E.

2.2 | Bending Self-Oscillation System

To evaluate the self-sustained oscillation performance, we systematically investigated the bending motion in a simplified system comprising an SF cantilever integrated with a magnetic patch laminated at one end (Figure 1A). As shown in Figure 2A, a typical oscillation cycle consists of three stages. To better understand the motion behavior in each stage, we recorded the displacement of the cantilever tip and calculated its velocity, acceleration, as well as the corresponding elastic and magnetic forces (Figure 2B, Text 1, Supporting Information). In the first stage, the SF cantilever bends toward the magnet from its original state under the attractive magnetic force between the driving module and the magnet. When the magnetic force applied to the CrO_2@SF begins to fall below the elastic force of the SF cantilever, the bending motion decelerates. In the next stage, as the driving module enters the light-illuminated region, the photothermal effect of CrO_2 causes the local temperature of the CrO_2@SF to rise. This temperature increase reduces the magnetization of CrO_2, further widening the gap between the elastic and magnetic forces. When the tip's velocity reaches zero, the deformation enters the third stage of the cycle, where the SF cantilever starts to rebound. In this final stage, the cantilever tip initially moves within the illuminated zone and then retracts out of it. The heated region cools quickly due to convective heat dissipation to the surrounding air. As the temperature drops, the magnetic susceptibility of CrO_2 recovers, which helps the magnetic force to exceed the decreasing elastic force. Eventually, the cantilever stops retracting and starts bending toward the magnet again, initiating the next oscillation cycle.

Leveraging the excellent photothermal response of CrO_2@SF and the high elasticity of the SF cantilever, this self-oscillating system enables rapid start/stop behavior (Figure 2C, Movie S3,). Upon activating the laser, the periodic oscillation stabilizes after only a few cycles. When the laser is turned off, the oscillation amplitude rapidly decreases and dampens to a full stop. This entire self-oscillating process was theoretically simulated, and the results were closely aligned with the experimental curve (Figure 2D, Text 2, Supporting Information). Following the rapid initiation, the stable oscillation dynamics are determined by the balance between F_M and F_E. The F_M, which is given by $F_M = m \times \nabla B$, depends on the spatial distribution of the magnetic flux (∇B) generated by the magnet and the magnetic moment (m) of the CrO_2@SF composite, which is temperature- and magnetic field-dependent ($m = (\chi < T, B > /\mu_0) \bullet B$, where χ is the local magnetic susceptibility, T is temperature, B is the external magnetic field, and μ_0 is permeability of vacuum). The F_E in the normal direction at beam tip deflection (w) is given by $F_E = Ebh^3w/4L^3$, determined by the cantilever's Young's modulus (E) and its geometry, including length (L), width (b), and thickness (h). Consequently, the oscillatory dynamics can be actively tuned either (i) through changing the external energy inputs, such as light field and magnetic fields, which modulate F_M photothermally, or (ii) by modifying material/geometric parameters to regulate F_E.

When the cantilever's material and geometry are fixed, the oscillation performance can be easily tuned by modulating the NIR laser intensity. The influence of laser intensity on the oscillation performance is depicted in Figure 2E. At relatively low laser intensities (<14.1 mW/mm^2), the deflection range increases remarkably as the intensity rises. This is because a higher intensity causes a greater temperature increase of the driving module, which leads to longer cooling times and allows for more rebound. Hence, the oscillatory amplitude is enhanced through the expansion of the upper bound of the bending angle (Figure 2E). In the intermediate laser power range (16.8–36.2 mW/mm^2), the upper bound continues to increase due to the increasing maximum temperature. However, the lower bound also increases with laser power, as rapid heating accelerates demagnetization of the driving module, triggering rebound at smaller deflections. As a result, the oscillation amplitude does not change significantly, but it shifts slightly closer to the cantilever's initial position (75°, Figure S7B). When the laser intensity exceeded 39.4 mW/mm^2, we observed large fluctuations in the oscillation amplitude with an unsteady cycle duration (Figure S8). This instability is likely due to excessive heating, which causes surface temperature fluctuation in the driving module. These fluctuations disrupt the periodic pattern of the magnetic and elastic forces, causing the system to enter a chaotic oscillation mode. In contrast to the amplitude, the oscillation frequency exhibits a monotonic decreasing trend with increasing laser power (Figure 2E). In addition, the oscillatory performance can be tuned by the magnetic field strength. Increasing the magnetic field enhances the F_M, leading to larger deformation and acceleration of the functional module, and consequently increasing both oscillation amplitude and frequency; conversely, whereas weaker fields produce the opposite effect (Figure S9).

Under constant external light and magnetic fields, both the oscillation amplitude and frequency can be tuned by modulating the geometrical parameters of the SF cantilever. As the length or thickness of the cantilever increases, the oscillation amplitude first increases and then decreases, while the frequency exhibits the opposite trend—initially decreasing and then partially recovering (Details see Figure S10). Figure 2F,G presents the maximum oscillation amplitude and frequency achievable by the system under different geometric parameters, obtained by optimizing the magnetic field strength and laser power for each configuration. In one extreme case where the cantilever is long (45 mm) and thin (35 µm), the elastic force is too weak to counteract the magnetic force, so no rebound occurs even after demagnetization. In the opposite extreme, where the cantilever is short (25 mm) and thick (75 µm), the magnetic force is insufficient to bend the cantilever, resulting in no observable deformation to begin with. In the parameter space between these two extremes, varying the length

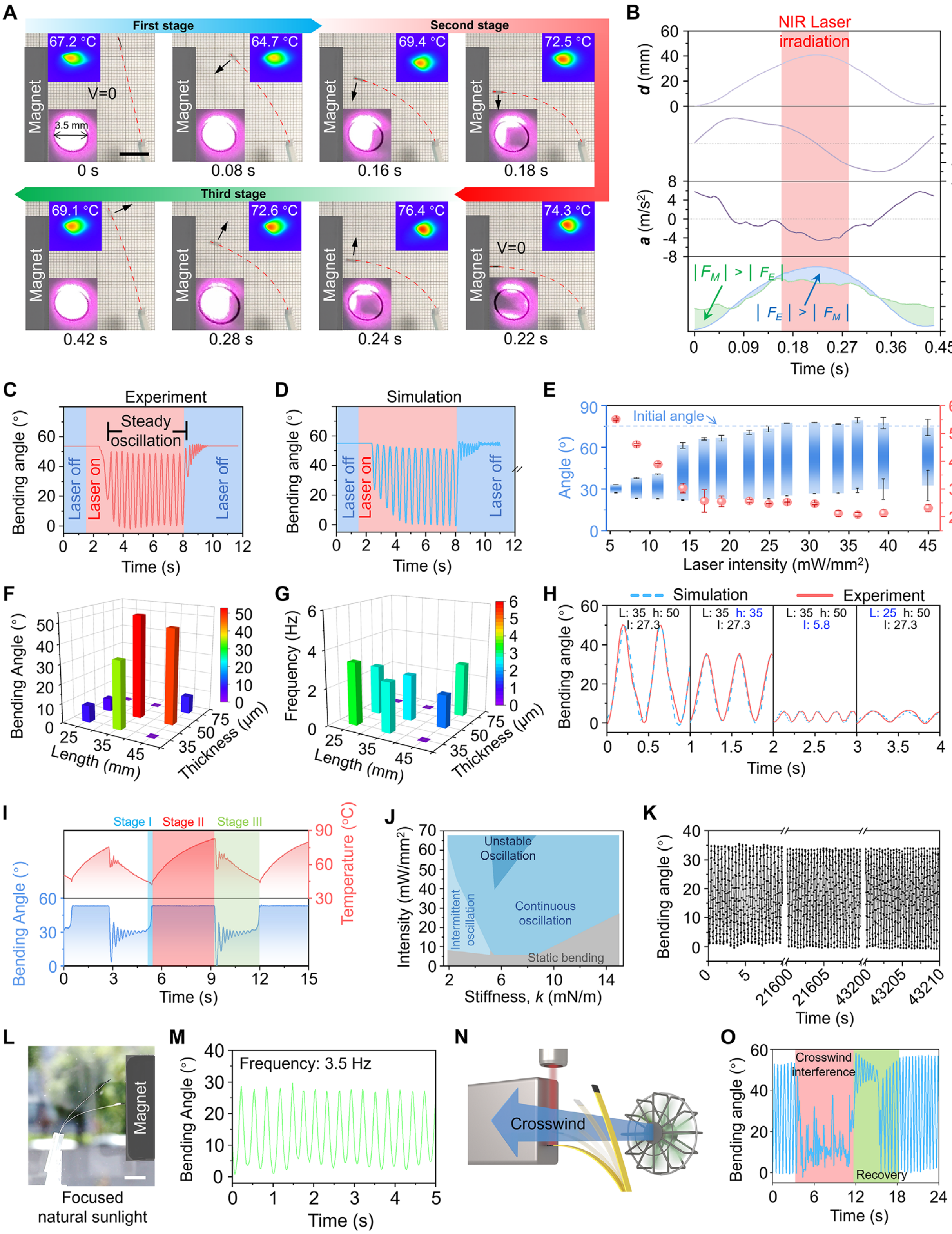

FIGURE 2 | Performance analysis of the bending self-oscillation system. (A) Snapshots of the bending oscillating motion in one cycle. Inset is the surface temperature and the projected cantilever tip on the NIR laser spot ($I = 27.3$ mW/mm^2). Unless otherwise noted, an SF cantilever measuring 35 mm in length, 3.5 mm in width, and 50 μm in thickness is positioned at an initial angle of 75°. (B) Recorded cantilever tip travel distance, calculated velocity, acceleration, magnetic force, and elastic force throughout one oscillation cycle. The red-shaded region denotes the time interval within a single oscillation cycle during which the driving module enters the laser spot. (C,D) Actuation performance throughout a complete self-oscillating process, from initiation to the cessation of oscillation, characterized by experiment (C) and simulation (D). The definition of the bending angle is illustrated in Figure S7A. (E) Oscillation angle range related to the horizontal reference (0°, Figure S7B) and frequency under various laser intensities. (F,G)

and thickness enables a wide range of oscillation amplitudes and frequencies, with maximum observed values of 52° and 3.3 Hz for bending angle and oscillatory frequency, respectively. Besides geometric parameters, the oscillation characteristics depend critically on the cantilever's orientation (Figure S11). The maximum oscillation amplitude increases with the initial angle, as a greater separation from the magnet allows more space for bending deformation during oscillation. However, the oscillation frequency displays a non-monotonic dependence on the initial angles, first increases, then decreases. This trend arises because, initially, a larger initial angle leads to a greater deflection, which enhances the rebound force and movement velocity, ultimately resulting in a higher frequency. As the initial angle continues to grow, the significantly enlarged amplitude prolongs the duration of each oscillation cycle, thus reducing the frequency. The oscillation amplitude and frequency under varying laser intensities and geometries were predicted by using finite element simulation. As shown in Figure 2H, the simulated results are in agreement with the experimental curves, confirming the system's responsiveness to changing conditions. Notably, although oscillation amplitude and frequency are coupled in the current single-magnet configuration, they can be effectively decoupled through a strategic arrangement of the external magnetic field (Details see Note S1). This capability represents a key distinction between the present system and conventional self-oscillating platforms.

To qualitatively understand how external energy inputs and geometrical parameters affect oscillation dynamics, we developed a theoretical model to predict the maximum amplitude $\theta_{\max}$ and frequency f (see more details in Text 3, Supporting Information), which can be expressed as:

$$\theta_{\max} = \frac{\omega}{\alpha\omega_k}\sqrt{\frac{(B_{\max} - B_{start}) \cdot m_0 \cdot L^2}{E \times b^3 \times h^2}}\, rad \tag{1}$$

$$f = \frac{\omega}{2 \times \omega_k}\sqrt{\frac{\nabla B_0 \times m_0}{2 \times L \times \theta_{max} \times G}} \tag{2}$$

where $B_{\max}$ and B_{start} denote as the maximum magnetic flux strength at the light-induced rebound position and the magnetic flux strength at the initial oscillation point; ∇B_0 is the gradient of the magnetic induction; m_0 is the original magnetic moment of CrO_2; G, L, E, b, and h represent the mass, length, Young's modulus, width, and thickness of the deforming module; α represents the coefficient of proportionality between the dynamic and static temperatures mentioned; ω and ω_k represent the experimental light intensity used for oscillation and the light intensity required to heat the material to the Curie temperature during static measurement; When $\omega > \omega_k$, take $\omega = \omega_k$ as the oscillatory frequency plateaus. To assess the consistency between theoretical predictions and experimental observations, we performed validation calculations using SF cantilevers of varying stiffness. The results demonstrate that the theoretical values are in good agreement with the experimental measurements (see case study in Text 3, Supporting Information for details). From the equation, it is evident that f is inversely proportional to the $\theta_{\max}$, which is also consistent with the experimental observations presented in Figure 2E. In practice, the oscillation performance of OMSOS can be further enhanced by systematically integrating and coordinating optimization strategies spanning photothermal efficiency, heat dissipation, magnetic force, and system architecture, thereby enabling an overall optimal oscillatory response (Details see Note S2).

In addition to performing continuous self-oscillation, intermittent oscillation (Figure 2I) can be achieved by reducing either the light intensity or the stiffness of the body material. The intermittent oscillation cycle comprises three distinct stages: (i) magnetically attracted bending, (ii) quasi-static heating, and (iii) rebounding with attenuated vibrations. With a smaller F_E generated by a less stiff body material, in order to still meet the condition $|F_E| > |F_M|$ for activating the retraction process, the magnetic component needs to undergo further demagnetization by reaching a higher temperature. Without increasing the NIR power, the magnetic component must be illuminated for a longer period to reach this elevated temperature. This extended heating time leads to the stationary deformation at the bent position. Once the magnetic force is reduced below the elastic force, the stored elastic energy is rapidly released, causing the cantilever to quickly rebound and undergo attenuated vibrations as it cools down and eventually comes to a stop. The interval between the attracted bending and rebound vibration can be shortened by increasing the NIR intensity (Figure S12). This unique oscillatory behavior, comprising two motion stages and a stationary stage, enables effective decoupling of amplitude and frequency (Note S1).

In Figure 2J, we summarize the experimental results of oscillation states under varying laser intensities and different stiffness levels of the deforming module. Steady oscillations occur over a wide range of laser intensities and material stiffnesses, whereas intermittent self-oscillations emerge in low-laser-intensity and low-material-stiffness regimes. Unstable oscillations primarily arise at high laser power and medium material stiffness. However, at low laser power, the system fails to generate oscillatory motion and instead exhibits only static bending due to insufficient demagnetization. Because the SF cantilever undergoes purely elastic deformation while the CrO_2@SF module reversibly demagnetizes and remagnetizes, the self-oscillation motion remains stable and repeatable for at least 12 h under continuous operation

---

The influence of deforming module geometries on the oscillation amplitude (F) and frequency (G) at a fixed initial angle of 75°. The amplitude and frequency for each size represent the maximum achievable value under the given conditions. (H) Oscillation profiles under varying geometries and laser intensities by experiment and simulation. (I) Bending angle and the corresponding surface temperature over time under the intermittent ($L = 45$ mm, $I = 5.86$ mW/mm^2) mode. (J) Oscillation states concerning the stiffness of the deforming module and laser intensities. Stiffness k is defined as $k = 3EI/L^3$, where $I = bh^3/12$, where E is Young's modulus, L is length, b is width, and h is thickness. (K) Bending oscillation recorded for over 43 210 s (12 h). Laser intensity of 14 mW/mm^2. (L) Overlayed photos showing the bending oscillation driven by focused natural sunlight ($I = 0.25$ mW/mm^2). (M) Recorded bending motion over time. (N) Schematic of the lateral airflow disturbance test of the OMSOS. (O) Dynamic response and autonomous recovery of OMSOS under external disturbance. Scale bars: 1 cm. Data in (E) are presented as mean ± SD, sample size $n = 5$.

(Figure 2K), demonstrating the system's durability and reliability for long-term use.

Since the photothermal effect of CrO_2 is not wavelength-specific, ubiquitous sunlight can effectively trigger the oscillation, greatly enhancing the versatility of the self-oscillation system. We first demonstrated continuous self-regulated oscillation using focused simulated sunlight (Figure S13 and Movie S4). In the intensity range from 0.063 to 0.6 mW/mm^2, the oscillation amplitude increases with higher sunlight intensity. However, when the light intensity surpasses a certain threshold, for example, when using 1 mW/mm^2, the amplitude begins to decrease due to overheating-caused fluctuations. Notably, the self-oscillation system operates effectively under a wide range of light incident angles (Figure S14). This means that, when using natural sunlight as the heating source, the system can operate over extended periods, as the solar angle changes throughout the day, rather than at a fixed time. We further demonstrated the utilization of focused natural sunlight to power the self-oscillation motion (Figure 2L and Movie S4), achieving an oscillation amplitude of 25.38° and frequency of 3.53 Hz (Figure 2M). In contrast, unfocused light illuminates the driving module constantly, though the light's incidental angle varies as the beam deflects, the heating effect is not different enough so that only chaotic oscillation occurs (Figure S15). Beyond sunlight-driven operation, the OMSOS exhibits pronounced resistance to external perturbations, such as strong lateral airflow (Figure 2N), and an ability to autonomously recover stable motion (Figure 2O), underscoring its potential for reliable operation in complex and fluctuating environments. Furthermore, when hygroscopic materials are used as functional modules, the system still exhibits good tolerance to environmental humidity fluctuations and strong performance recoverability: upon returning to the initial humidity level, the oscillatory behavior is largely restored (Figure S16).

2.3 | Self-Oscillation Systems With Broad Materials and Configurations

The modular design of the OMSOS system significantly broadens the design space for material selection. To enable self-oscillation across different material compositions, it is essential that their stiffness—governed by Young's modulus and geometric dimensions—falls within an appropriate range, as shown in Figure 2J for an exemplary cantilever system. This stiffness window allows for the systematic determination of compatible dimensional parameters for any given material system. Using the stiffness boundary values identified in Figure 2J, we calculated the range of geometric parameters (A, defined as $bh^3/4L^3$, see Text 4, Supporting Information for details) capable of sustaining continuous self-oscillations for materials with varying Young's moduli (Figure 3A). To validate these calculations, we selected six representative body materials spanning seven orders of magnitude in Young's modulus as the deformation modules to construct OMSOS systems. Experimental measurements confirmed that all fabricated samples exhibited sustained self-oscillatory motion (Figure S17 and Movie S5), in agreement with the predictions.

In addition to material versatility, this system also enables flexible configuration design and adaptive oscillatory modalities that transcend the simple bending mode of conventional cantilever-beam architectures. Using SF films as the core material for the deforming module, we demonstrate a library of reconfigurable self-oscillating systems capable of diverse architectures and multimodal dynamics (Movie S6). First, we constructed an SF spring architecture to generate vertical up-and-down self-oscillation (Figure 3B), driven by a balanced extension-heat-demagnetize-retraction-cool-extension cycle. Next, we suspended an SF disk using an SF ribbon and integrated two 4-layered CrO_2@SF films at both ends of the diameter to enable a large-amplitude rotational oscillation (Figure 3C). Additionally, we demonstrated a pendulum-like setup where the interplay of magnetic and gravitational forces induces a swinging motion (Figure 3D). The configurational flexibility of OMSOS also enables synergistic coupling of multiple motion modalities. For instance, a helical-shaped SF ribbon allows both vertical stretching and horizontal twisting oscillations (Figure 3E). In a different design, combining an SF spring with two SF cantilevers produces coupled up-and-down and bending oscillations (Figure 3F). Beyond continuous self-oscillation, these modes can operate in intermittent regimes (Figure S18), introducing an additional control dimension for dynamic motion manipulation. A fundamental requirement for sustaining self-oscillation across all modes is that the light spot must remain smaller than the driving module's displacement range, ensuring the module can move away from the light during oscillation. When satisfied with proper architectural designs, diverse self-oscillation modes beyond those demonstrated in this work become achievable.

2.4 | Self-sustained dynamic Optical Display and Scanning Systems

Being capable of decoupling the deforming module from the driving module transforms the design paradigm for self-oscillating systems, shifting from integrated monolithic systems to modular, customizable (plug-and-play) component systems. This architectural flexibility significantly expands the application scope of OMSOS, enabling functionalities that are not equipped by existing self-oscillation systems. By integrating optical components directly with the deforming modules, this framework allows for the real-time reconfiguration of light–matter interactions, providing a versatile platform for self-sustaining, dynamic optical displays. To demonstrate this capability, we developed passive dynamic structural color and holographic display devices through precisely engineering the surface topography of a bending-mode deforming module. The SF film was selected as the deforming module due to its exceptional compatibility with nano-imprinting techniques, allowing for high-precision fabrication and integration of optical structures [40, 41].

Leveraging the angle-dependent optical response of grating structures, we demonstrated a dynamic structural-color-based display using OMSOS. We imprinted two patterned diffractive gratings with different periods on the two surfaces of an SF cantilever (Figure 4A). Since gratings of different periods exhibit distinct angle ranges for visualization [40], we could achieve reversible pattern switching by optimizing the bending oscillation amplitude according to the grating angles. As shown in Figure 4B, the bending motion first caused a blue shift in the color of the "SILK" pattern and then switched to show the "CrO_2" pattern, which

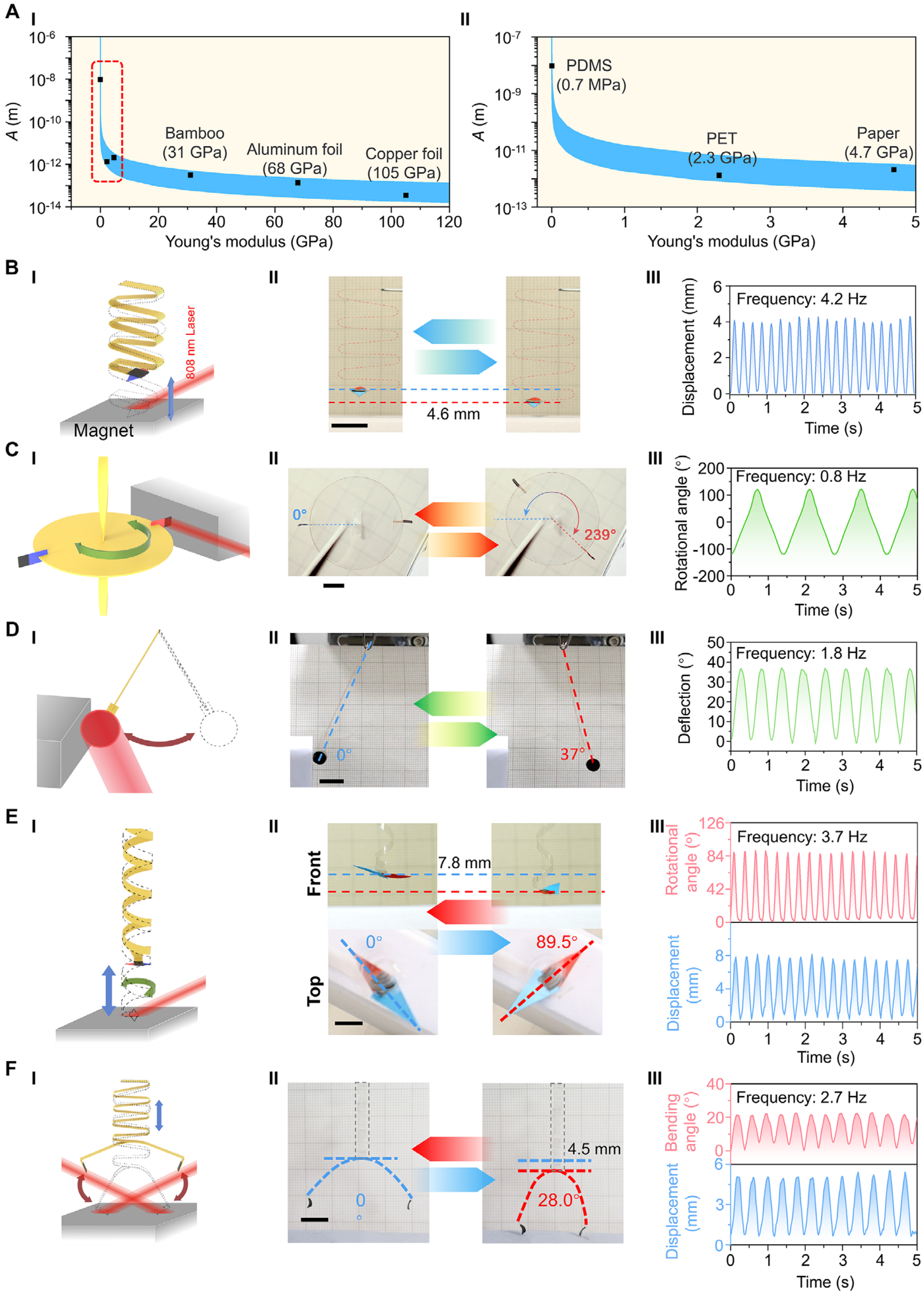

FIGURE 3 | Versatility of OMSOS in materials, configurations, and oscillation modes. (A) Material-dependent conditions for achieving continuous self-oscillation. (I) Calculated A value as a function of Young's modulus (blue-shaded area) and experimentally validated data points corresponding to materials with different moduli that are capable of sustaining self-oscillations (points). (II) Enlarged plot of the red box in (I). (B–F) Self-oscillation systems with different configurations and modes: (B) an SF spring architecture for up-and-down oscillation, (C) An SF ribbon suspended from the center of an SF disc for rotational oscillation, (D) A pendulum-like setup for swinging oscillation, (E) A helical-shaped SF ribbon for a complex oscillation that combines up-and-down and twisting oscillations, (F) A SF spring combined with two SF cantilevers for a complex oscillation that combines bending and up-and-down oscillations. (I–III, in B–F) Set-up (I), oscillation snapshot (II), and the corresponding trajectory analysis (III) of each configuration. The NIR laser intensity is 20 mW/mm^2 for up-and-down and complex mode in (E), 51 mW/mm^2 for rotation mode, 15 mW/mm^2 for swing mode, and 25 mW/mm^2 for complex mode in (F). Scale bars: 1 cm.

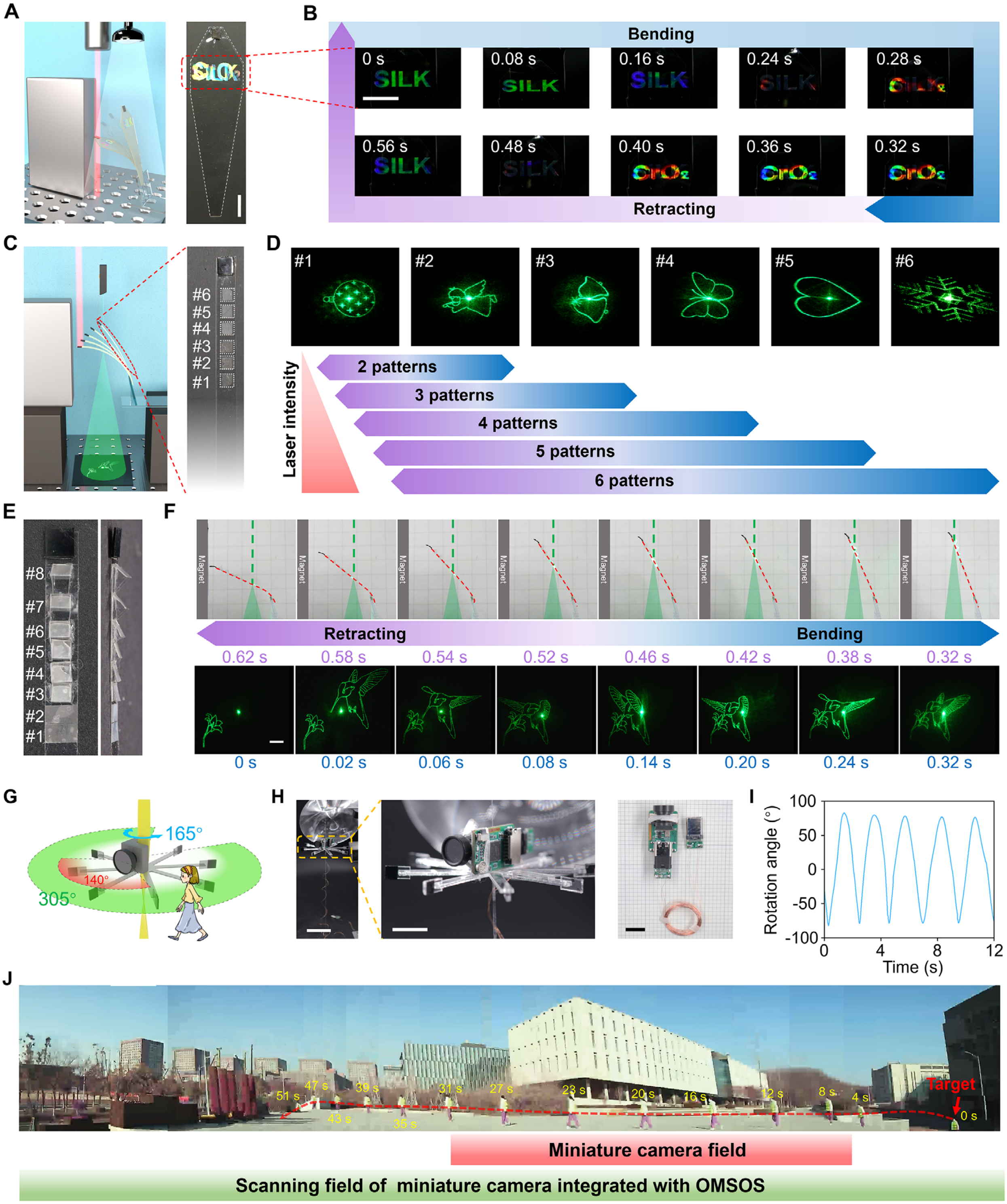

FIGURE 4 | Dynamic optical display systems. (A) The setup for the dynamic structural color display and a photograph of the corresponding device. (B) Photo series of information switches in one oscillation cycle. NIR laser intensity is 22.5 mW/mm^2. (C) The setup for a dynamic holographic display and a photograph of the corresponding self-oscillating device. (D) Photo series showing the customizable switching between different combinations of DOE diffraction patterns via laser intensity modulation. (E) Photographs showing the device for a holographic animation display. To mitigate irradiation-angle-dependent effects on the diffraction pattern, the imprinted SF DOEs were mounted onto an SF cantilever at different angles (see Figure S20 for details). (F) Photo series showing the bending motion over time during one oscillation cycle along with the corresponding holographic animation keyframes. NIR laser intensity is 27.3 mW/mm^2. (G) Schematic of the wide-area camera scanning setup, in which a miniature camera is integrated onto the OMSOS to achieve oscillatory scanning. (H) Photographs of the experimental setup (left) and a camera connected to a battery (right). (I) Trajectory analysis of the oscillatory scanning system actuated by focused natural sunlight. (J) Photographs demonstrating real-time security monitoring of a restricted building using the OMSOS-integrated scanning system. Scale bars: 1 cm (B,F,H-middle,H-right), 3 cm (H-left).

similarly underwent a blue shift. During the return motion, this optical transformation sequence is reversed (Movie S7).

The OMSOS also enables dynamic far-field holographic display capabilities. To demonstrate this functionality, we fabricated an array of diffractive optical elements (DOEs) directly on the SF cantilever via nanoimprint lithography (Figure 4C). During the self-regulated bending motion, a 523 nm laser (for display-only) sequentially illuminated different DOE zones, projecting time-multiplexed holographic images onto the screen below (Figure 4D). The dynamic mechanical deformation enables autonomous pattern switching without additional control inputs. The frame rate of the display (patterns per oscillation cycle) can be controlled by modulating the intensity of the NIR heating laser, enabling adaptive holographic display without system reconfiguration (Movie S8). Furthermore, self-looping holographic animation playback can be achieved using this approach by sequentially encoding stop-motion keyframes onto the deforming module. As a proof-of-concept, we developed a holographic animation system depicting a hummingbird feeding from a flower, with each DOE encoding a discrete frame of the animation (Figure 4E). During bending oscillation, the system's large and controllable amplitude, combined with its optimal oscillation frequency, enabled high-quality reciprocal animation playback with distinguishable keyframes and smooth motion perception (Figure 4E, Movie S9). This mechanical oscillation system establishes a new, low-cost strategy for creating persistent-of-vision displays through controlled structural dynamics.

Beyond dynamic optical displays based on bending oscillations, the rotational self-oscillation system offers further advantages. Its inherent configurability—including on-demand reconfiguration of deforming components and integration schemes—combined with large-amplitude motion, makes it particularly suitable for wide-angle optical scanning applications. In one such demonstration, a miniature camera was integrated into a self-oscillating rotational system to realize a cost-effective, remotely controlled, and wide-area visual scanning system. The self-oscillating system is easy to set up: CrO_2@silk films were welded to plastic patches and mounted onto each leg of an eight-legged plastic load platform with a miniature camera via a tenon-and-mortise structure, which was then mounted on an elastic SF ribbon (Figure 4G,H; Figure S19). The camera module is powered via a Type-C interface (Figure 4H). Power is supplied through a 0.1-mm-diameter enameled copper wire helically wrapped around the central elastic strip, preserving the self-oscillating rotational motion while ensuring a stable and continuous external power supply. Despite the additional payload of the micro-camera (3.5 g), large-amplitude oscillation is preserved by increasing the number of driving modules to compensate for the added inertia. Under focused sunlight illumination, the system maintains an oscillation amplitude of 165° (Figure 4I), thereby expanding the effective surveillance coverage from 140° to 305° (Figure 4G). With this setup, we constructed a security monitoring scenario (Figure 4J and Movie S10), in which OMSOS-mounted cameras perform continuous real-time surveillance around a restricted building. Owing to the wide-angle oscillatory motion, the camera coverage fully encloses the building perimeter, enabling comprehensive tracking of moving objects and early identification of potential security risks. Furthermore, the swinging oscillation mode of the OMSOS can be utilized to construct a laser modulator by leveraging the laser as both the excitation source and the modulation output, enabling autonomous, motion-encoded photo-thermal modulation (Note S3).

2.5 | Self-Oscillating Electricity Generator

The OMSOS system can be reconfigured to apply for highly efficient, sustained electrical energy harvesting. To demonstrate this capability, we incorporated a commercially available piezoelectric and pyroelectric PVDF membrane into the OMSOS system as the deforming module. As illustrated in Figure 5A, the self-oscillation generator was assembled by coating the PVDF membrane with aluminum electrodes on both sides and moisture-welding a 4-layer CrO_2@SF patch to its tip. The generator was electrically connected to a load resistor for energy conversion analysis (Figure S21). Under bending oscillatory motion, the voltage output is generated through both the piezoelectric effect induced by dynamic strain variations across the entire PVDF cantilever and the pyroelectric effect [42]. (Figure 5B) resulting from dynamic temperature fluctuations localized at the cantilever's tip. To assess the performance, we compared the generated voltages from continuous and intermittent self-oscillation modes (Figure 5C). The intermittent mode exhibits significantly higher peak output voltages (+10.5 and −12.3 V at 1 GΩ load, Figure 5D) than the continuous mode (Figure S22). To maximize the electrical output, we employed the intermittent self-oscillation mode for this energy harvesting system. To decouple the contributions of piezoelectric and pyroelectric effects, we replaced the welded connection with a short SF filament, thermally isolating the magnetic/heating module from the PVDF cantilever. This design ensures that the measured peak output (+127 and −97 mV, Figure 5C; Figure S23) stems solely from mechanical bending (piezoelectric effect). Notably, this signal is three orders of magnitude lower than the combined pyroelectric–piezoelectric output, demonstrating that the pyroelectric effect dominates the overall electricity generation in our system.

To elucidate the high-voltage generation mechanism during intermittent self-oscillation, we systematically analyzed the interplay between output voltage, bending angle, and temperature dynamics. Our analysis reveals three distinct voltage generation stages within each oscillation cycle, each corresponding to specific variations in bending angle and temperature (Figure 5E). We learned that the voltage generation is mainly contributed by the heating/cooling pyroelectric effect. In pyroelectric systems, the output voltage scales proportionally with the rate of temperature change (dT/dt) [43]. In the maximum bending and static heating stage (red shaded zone, first stage), a sharp temperature increase generates a high positive (+) voltage, and it rises to a gradual plateau as heating slows down; in the rebound and dynamic cooling stage (dark blue shaded zone, second stage), the damped oscillation enhances thermal convection, accelerating cooling of the PVDF membrane and leading to a swift transition to negative (−) voltage output; and in the static cooling stage (light blue shaded zone, third stage), the slower, steady cooling rate results in gradually stabilizing voltage output variations. Further analysis reveals that intermittent self-oscillation achieves significantly larger temperature gradients and faster temperature change rates compared to continuous operation, thereby accounting

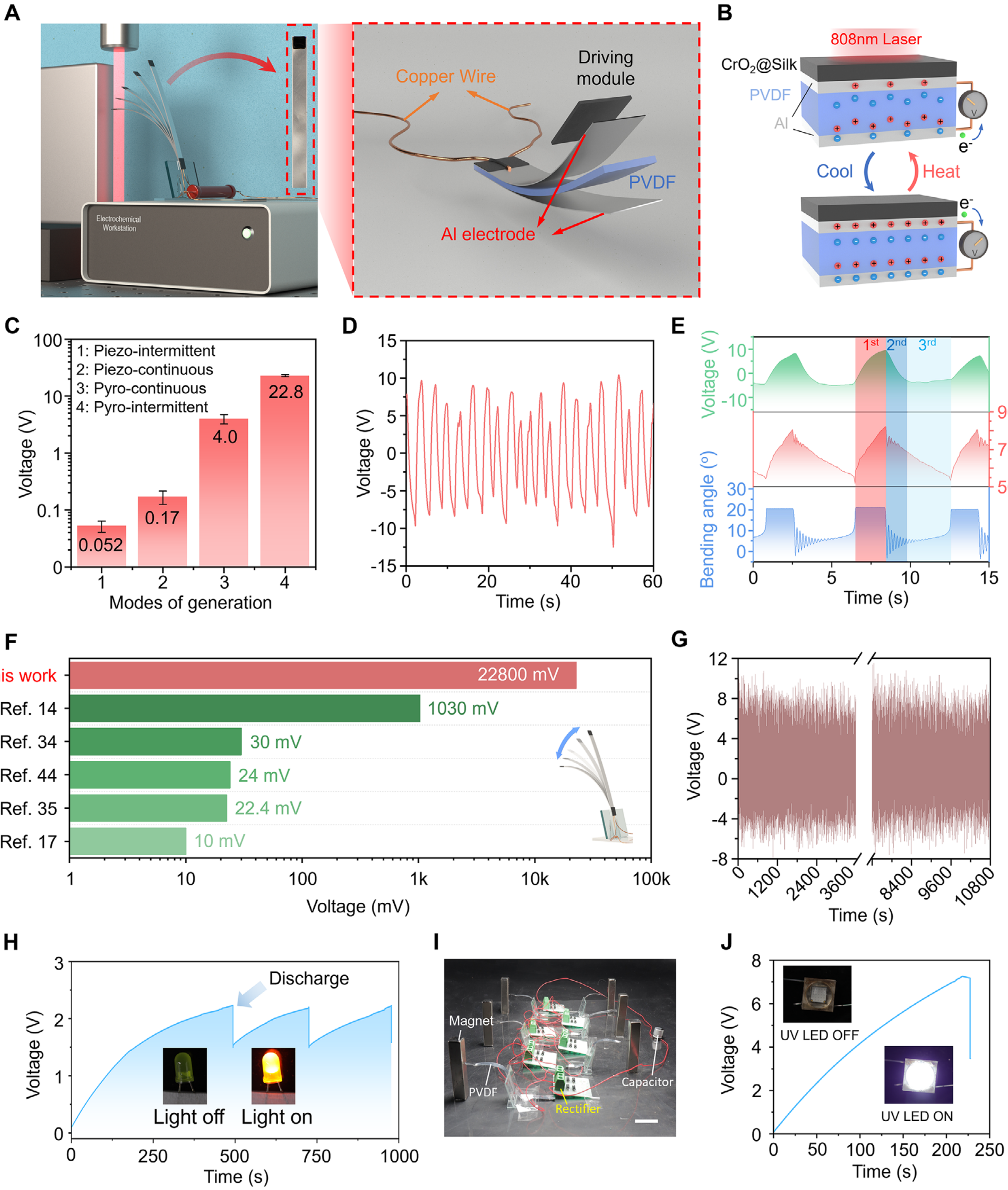

FIGURE 5 | Autonomous energy harvesting using self-sustained PVDF oscillators. (A) The setup and composition of the energy harvester. PVDF membrane dimensions: 45 mm (length) × 4 mm (width) × 50 µm (thickness). (B) The pyroelectric mechanism of the PVDF membrane. Temperature variations in PVDF induce a redistribution of internal charges, which creates a surface potential difference that generates measurable electrical signals through an external circuit. (C) The comparison of the peak output voltage of different generation modes. (D) The voltage output of the OMSOS generator with a 1 GΩ load resistor in an intermittent bending self-oscillation mode ($I = 55$ mW/mm^2). (E) The correlation among output voltage, surface temperature, and bending angle in the PVDF energy harvester. The shaded zones indicate the bending and heating (red, first), rebound and dynamic cooling (dark blue, second), and static cooling (light blue, third) stages, respectively. (F) Comparison of output voltages between bending-mode self-oscillating energy-harvesting systems. (G) The stable voltage output over a 10 800-s test period. (H) Charging and discharging curves of the tandem capacitor (4.7 µF), with insets showing an LED (working voltage: 1.8 V) illuminated during the capacitor discharge. (I) Photograph of an energy-harvesting system with six energy-conversion units connected in series. (J) Charging and discharging curves of the tandem capacitor (4.7 µF), with insets showing a UV LED (working voltage: 3.7 V) illuminated during the capacitor discharge. Scale bar: 2 cm. Data in (C) are presented as mean ± SD, $n = 5$.

for its enhanced voltage generation performance (Figure S24). Remarkably, its output voltage surpasses that of other bending-mode self-oscillating energy-harvesting systems by at least two orders of magnitude [14, 17, 34, 35, 44] (Figure 5F).

With its high peak output voltage, this self-oscillating electrical generator generated an average output power of 54.7 nW and cumulative output electric energy of 44.3 µJ in 1800 s (Figure S25). In addition, the self-oscillating generator demonstrated excellent operational stability, maintaining consistent performance without significant degradation during continuous operation for over 3 h (Figure 5G). Notably, by directly replacing the NIR source with sunlight, this system enables fully autonomous, zero-energy operation through self-oscillation-assisted solar-thermal-electric conversion. Under comparable incident light power densities, the output voltage generated by sunlight-driven operation is comparable to those obtained under laser excitation (Figure S26). The harvested electrical energy can be efficiently rectified and stored in a capacitor and subsequently used to power a light-emitting diode (Figure 5H). What's more, by connecting multiple energy-conversion units in series (Figure 5I), the output voltage can be further amplified (Figure S27). After energy storage, the harvested electrical power is sufficient to drive LED with higher operating voltage; for example, the system successfully powers a UV LED with a nominal operating voltage of 3.7 V (Figure 5J). Together, these results demonstrate the excellent scalability and practical feasibility of the OMSOS-driven energy-harvesting system as a self-sustained power-supply platform.

3 | Conclusion

In summary, we have developed a wirelessly activated, modularly assembled self-oscillation system through the synergistic application of unmodulated light and magnetic fields. By decoupling the active driving components and the passive deforming components, this OMSOS system addresses key limitations of current self-oscillation platforms, which require the deformation structures to be composed primarily or entirely of irreplaceable active components. This modular design paradigm unlocks unprecedented programmability in system composition, geometric configuration, deformation modes, and functional versatility. These capacities, along with wavelength-independent light actuation, allow the OMSOS system to adapt to diverse operational environments and application scenarios beyond the presented prototype implementations. Additionally, the ability to construct complex 3D configurations of the driving module enables the generation of spatially coupled and highly intricate oscillatory behaviors that are unattainable with conventional designs. This optically-induced demagnetization strategy enables precise microscale self-oscillation control and opens up new possibilities for seamless integration of micro-oscillators with various advanced technological platforms, including IR metamaterials, optical microcavities, sensor chips, and bioimaging devices. Through strategic improvement of the driving module's energy conversion efficiency and rational optimization of the system configuration, higher oscillation performance can be achieved using excitation light sources of lower power, which will enable more effective functional implementation and enhance overall practical applicability. The outlined strategy bridges critical gaps in current artificial self-oscillation systems and establishes a versatile framework for developing novel dynamic, adaptive, and intelligent systems that can leverage these automatic actuation mechanisms for advanced applications.

4 | Experimental Section

4.1 | Preparation of Regenerated Silk Fibroin (SF) Solution

SF was extracted from Bombyx mori silkworm cocoons. The aqueous SF solution was prepared using the method described in previous studies [45]. Briefly, silk cocoons were cut into smaller pieces and boiled in a Na_2CO_3 solution (0.02 M) for 30 min to remove the sericin layer. Following drying at room temperature for 2 days, the degummed SF fibers were dissolved in a LiBr solution (9.3 M) at a silk-to-LiBr solution ratio of 20% wt/vol at 60°C for 4 h. After dialyzing against deionized water for 3 days to remove the salt, and centrifuging at 11 000 rpm for 20 min to eliminate impurities, the final silk fibroin aqueous solution (~65 mg mL^{-1}, slightly varying from batch to batch) can be obtained.

4.2 | Pretreatment of Chromium Dioxide (CrO_2)

The method used to chemically passivate the as-received CrO_2 powder (Aladdin, Shanghai, China) was adapted from a previous study (39). CrO_2 powder was first ball-milled at 1500 rpm for 2 h to achieve a smaller and more uniform particle size distribution. CrO_2 particles (0.4 g) were suspended in ethanol (80 mL) for 5 min of ultrasonication, then ammonia (28% in water, 6 mL) was added to the mixture. Under vigorous stirring (300 rpm), a TEOS-ethanol solution (2% vol/vol, 20 mL) was slowly added dropwise to the suspension and left to react for 3 h. Silica-coated CrO_2 powder can be obtained after filtering the reacted suspension, washing it with ethanol 3 times, and subsequently drying it in an oven at 60°C

4.3 | Fabrication of CrO_2@SF Films

After being sonicated for 10 min, the pretreated CrO_2 power/water suspension (0.2 g mL^{-1}) was added into aqueous SF solution, with a CrO_2 to SF mass ratio of 1:1. The well-mixed CrO_2/SF suspension was quickly cast onto a silicon wafer that was pretreated by trichloro (1H, 1H, 2H, 2H perfluorooctyl) silane. The freestanding CrO_2@SF film was obtained after drying in a closed chamber (25°C and 50% RH) for 24 h.

4.4 | Fabrication of the Driving Module

CrO_2@SF film pieces (3.5 mm × 3.5 mm, unless otherwise specified) were fabricated using a laser cutter (Speedy 100R, Trotec Laser, Austria). A cut piece was sprayed with water mist on its SF-enriched surface for 3 s, then rapidly pressed onto the CrO_2-enriched side of another piece and left to dry before release. This procedure was repeated until four layers of CrO_2@SF films were welded together, forming the driving module.

4.5 | Assembly of The Self-Oscillation Systems

4.5.1 | Bending Self-Oscillation

The driving module was exposed to water mist for 3 s, then quickly pressed onto the tip of a designated cantilever beam (SF film or PVDF), and released after drying.

4.5.2 | Up-and-Down Oscillation

SF strips (80 mm × 3.5 mm × 50 μm) were cut and wrapped into “snake-shaped” grooves made of polydimethylsiloxane (PDMS). The assembled structure was placed in an environment of 45°C and 100% RH for 1 min to absorb water and undergo plasticization. Afterward, it was removed and dried under ambient conditions (25% RH) for 2 h to form the SF spring architecture. Finally, the CrO_2 driving module was welded to one end using water vapor to construct the up-and-down self-oscillating system.

4.5.3 | Rotational Oscillation

An SF disc (40 mm in diameter, 100 μm thick) was laser-cut, with openings created at the center and both lateral ends. An SF strip (20 cm × 1 mm × 30 μm) was threaded through the central opening, and an L-shaped SF film (3.5 mm × 5 mm) was used as a welding patch to secure the strip to the disc. The notches at the disc's ends were inserted into a small driving module assembly, which was pre-fabricated by welding the driving module to a silk film (8 mm × 3.5 mm × 100 μm) featuring an end notch.

4.5.4 | Swinging Oscillation

A lollipop-shaped SF film (disc diameter: 10 mm; rectangular handle size: 10 mm × 5 mm; thickness: 100 μm) and an SF strip (50 mm × 5 mm × 100 μm) were prepared, each containing a notch at one end. A driving module and a 1 mm-thick PMMA sheet (0.3 g) with a matched size to the disc were symmetrically welded to opposite sides of the disc. This assembled structure was then connected to the SF strip via the notch. The complete assembly was mounted onto a 1 mm-diameter metal shaft and positioned within a U-shaped metal ring to construct the self-oscillating system.

4.5.5 | Up-and-Down and Rotational Oscillations

An SF strip (80 mm × 3.5 mm × 50 μm) was spiral-wound onto a glass rod with a 5 mm diameter, and the pitch was adjusted and fixed. The assembly was then plasticized via 45°C water vapor fumigation for 1 min, removed, and dried under ambient conditions for 2 h to form a stable spiral SF film. Finally, a driving module was welded to one end of the spiral to construct the self-oscillating system.

4.5.6 | Bending and up-and-Down Oscillations

An SF spring structure was prepared, and an SF strip (3.5 mm × 50 mm × 50 μm) was welded to one end of the spring structure, followed by the attachment of driving modules to both ends of the strip. After water vapor treatment, the driving modules were bent inward at 90° and secured to finalize the self-oscillating system.

4.6 | Fabrication of DOE Devices

The DOE devices were fabricated by a laser direct writing system. A glass substrate with a thickness of 3 mm was pre-cleaned and spin-coated with a layer of positive photoresist (RJZ-390, RUIHONG Electronics Chemicals, China) at a thickness of 1 μm. The glass plate was then patterned by a homemade lithography system (Miscan, SVG Optronics, China) at a speed of 40 mm^2/min. The glass plate was developed in NaOH solution (8%) for 30 s. Finally, the glass plate was post-baked for 1 h. For mass production, the surface relief nanostructures on the glass plate can be further imprinted at low cost with high efficiency.

4.7 | Imprinting of SF Films

SF film patterning was performed using the previously reported micro- and nanoimprinting method [40]. In brief, an SF film cut into the desired shape was placed on a clean PDMS substrate, covered with a PDMS mask containing the target macro pattern, and exposed to water vapor at 45°C for 30 s. After stencil removal, a grating (period: 600 or 1200 grooves/mm) or a DOE master was immediately pressed onto the wetted film surface under constant pressure. Once dried, the master was carefully removed, leaving a replicated optical structure on the film surface.

4.8 | Characterization

The cross-sectional morphologies of the CrO_2@SF films were examined using a field-emission scanning electron microscope (S-8100, Hitachi, Japan). The hysteresis loops of silica-coated CrO_2 particles at 300 K were measured using a vibrating sampling magnetometer (Physical Property Measurement System, PMMS-9, Quantum Design, Inc., USA) under an external magnetic field range of −30–30 kOe. During the M–T measurements, the magnetic moment was measured from 200 to 400 K under an external magnetic field of 5 kOe. The light source used to heat the driving modules is an NIR (808 nm) continuous-wave laser (MDL-H-808-5 W, Changchun New Industries Optoelectronics Tech. Co. Ltd., China). The collimated laser beam was defocused using a lens of 3 cm focal length to expand the beam diameter to 5 mm. The total output power of the NIR laser was measured using an optical power meter (PM100A, Thorlabs GmbH, Germany). The temperature profile measurement or thermal image capturing was performed by an IR camera (628C, Forric, China). Since the temperature profile was not spatially uniform across the sample, the maximum temperature was recorded. Photographs were taken with a digital single-lens reflex camera (EOS 850D, Canon), and videos were taken at a framerate of 30 fps. The trajectory of the oscillators was analyzed using Tracker (open-source, version 6.1.3) to track the beam tip position in each frame, from which the amplitude and frequency were determined. The far-field diffraction information was extracted by propagating a green laser (2802, deli, China) with a wavelength range of 500–552 nm through the imprinted SF film. The output voltage of the PVDF (Jinzhou KEXIN Electronic Material Co., Ltd., China) self-oscillation generator was measured using an electrochemical workstation (VSP-300, BioLogic, France) in adapted mode with a sampling rate of 10 points per second.

Author Contributions

Y.-Q.L., Y.W., M.L. and Y.-H.F. conceived the idea and designed the research. Y.-H.F., Z.-T.W. and T.W. performed the experiments. A.P. assisted in the theoretical analysis. Y.-H.F., Y.W. and M.L. analyzed the experimental data. Y.-Q.L., Y.W., M.L., W.Q., X.S.Q. and Y.-H.F. wrote and revised the manuscript. Y.-Q.L. and Y.W. supervised the research. All authors approved the final version of the manuscript.

Acknowledgements

This work was supported by the National Key R&D Program of China (Nos. 2022YFA1203702 and 2022YFA1405000), the National Natural Science Foundation of China (Nos. 62175102 and T2488302), the Natural Science Foundation of Jiangsu Province (No. BK20243067), and the Shanghai Jiao Tong University SiYuan Scholar Program.

Conflicts of Interest

The authors declare no conflict of interest.

Data Availability Statement

The data that support the findings of this study are available from the corresponding author upon reasonable request.

References

1. D. Wang, Z. Chen, M. Li, et al., “Bioinspired Rotary Flight of Light-Driven Composite Films,” *Nature Communications* 14 (2023): 5070, https://doi.org/10.1038/s41467-023-40827-4.

2. J. Yang, M. R. Shankar, and H. Zeng, “Photochemically Responsive Polymer Films Enable Tunable Gliding Flights,” *Nature Communications* 15 (2024): 4684, https://doi.org/10.1038/s41467-024-49108-0.

3. W. Hu, G. Z. Lum, M. Mastrangeli, and M. Sitti, “Small-Scale Soft-Bodied Robot With Multimodal Locomotion,” *Nature* 554 (2018): 81–85, https://doi.org/10.1038/nature25443.

4. M. Li, A. Pal, A. Aghakhani, A. Pena-Francesch, and M. Sitti, “Soft Actuators for Real-World Applications,” *Nature Reviews Materials* 7 (2022): 235–249, https://doi.org/10.1038/s41578-021-00389-7.

5. H. Yang, X. Yin, C. Zhang, B. Chen, P. Sun, and Y. Xu, “Weaving Liquid Crystal Elastomer Fiber Actuators for Multifunctional Soft Robotics,” *Science Advances* 11 (2025): ads3058, https://doi.org/10.1126/sciadv.ads3058.

6. C. Chen, P. Shi, Z. Liu, et al., “Advancing Physical Intelligence for Autonomous Soft Robots,” *Science Robotics* 10 (2025): ads1292, https://doi.org/10.1126/scirobotics.ads1292.

7. Z.-Z. Nie, M. Wang, and H. Yang, “Self-Sustainable Autonomous Soft Actuators,” *Communications Chemistry* 7 (2024): 58, https://doi.org/10.1038/s42004-024-01142-1.

8. K. Kumar, C. Knie, D. Bleger, et al., “A Chaotic Self-Oscillating Sunlight-Driven Polymer Actuator,” *Nature Communications* 7 (2016): 11975, https://doi.org/10.1038/ncomms11975.

9. Y. Zhao, Q. Li, Z. Liu, et al., “Sunlight-Powered Self-Excited Oscillators for Sustainable Autonomous Soft Robotics,” *Science Robotics* 8 (2023): adf4753, https://doi.org/10.1126/scirobotics.adf4753.

10. F. Zhai, Y. Feng, Z. Li, et al., “4D-Printed Untethered Self-Propelling Soft Robot With Tactile Perception: Rolling, Racing, and Exploring,” *Matter* 4 (2021): 3313–3326.

11. D. S. Kim, Y.-J. Lee, Y. B. Kim, Y. Wang, and S. Yang, “Autonomous, Untethered Gait-Like Synchronization of Lobed Loops Made From Liquid Crystal Elastomer Fibers via Spontaneous Snap-Through,” *Science Advances* 9 (2023): adh5107, https://doi.org/10.1126/sciadv.adh5107.

12. Z. Li, N. V. Myung, and Y. Yin, “Light-Powered Soft Steam Engines for Self-Adaptive Oscillation and Biomimetic Swimming,” *Science Robotics* 6, no. 6 (2021): abi4523, https://doi.org/10.1126/scirobotics.abi4523.

13. R. K. Manna, O. E. Shklyaev, and A. C. Balazs, “Chemical Pumps and Flexible Sheets Spontaneously Form Self-Regulating Oscillators in Solution,” *Proceedings of the National Academy of Sciences* 118 (2021): 2022987118, https://doi.org/10.1073/pnas.2022987118.

14. T. Mao, Z. Liu, X. Guo, et al., “Engineering Covalent Organic Frameworks With Polyethylene Glycol as Self-Sustained Humidity-Responsive Actuators,” *Angewandte Chemie International Edition* 62 (2023): 202216318, https://doi.org/10.1002/anie.202216318.

15. Y. Zhao, C. Xuan, X. Qian, et al., “Soft Phototactic Swimmer Based on Self-Sustained Hydrogel Oscillator,” *Science Robotics* 4 (2019): aax7112, https://doi.org/10.1126/scirobotics.aax7112.

16. Z. Deng, H. Zhang, A. Priimagi, and H. Zeng, “Light-Fueled Nonreciprocal Self-Oscillators for Fluidic Transportation and Coupling,” *Advanced Materials* 36 (2024): 2209683, https://doi.org/10.1002/adma.202209683.

17. Y. Zhao, Z. Liu, P. Shi, et al., “Antagonistic-Contracting High-Power Photo-Oscillators for Multifunctional Actuations,” *Nature Materials* 24 (2025): 116–124, https://doi.org/10.1038/s41563-024-02035-3.

18. R. Lan, J. Sun, C. Shen, et al., “Near-Infrared Photodriven Self-Sustained Oscillation of Liquid-Crystalline Network Film With Predesignated Polydopamine Coating,” *Advanced Materials* 32 (2020): 1906319, https://doi.org/10.1002/adma.201906319.

19. X. Che, T. Wang, B. Zhang, et al., “Two-Dimensionally Nano-Capsulating Liquid Metal for Self-Sintering and Self-Oscillating Bimorph Composites With Persistent Energy-Harvest Property,” *Advanced Functional Materials* 34 (2023): 2307830, https://doi.org/10.1002/adfm.202307830.

20. X. Q. Wang, C. F. Tan, K. H. Chan, et al., “In-Built Thermo-Mechanical Cooperative Feedback Mechanism for Self-Propelled Multimodal Locomotion and Electricity Generation,” *Nature Communications* 9 (2018): 3438, https://doi.org/10.1038/s41467-018-06011-9.

21. X. Li, P. Huang, B. Li, et al., “Adaptive Multi-Degree of Freedom Self-Oscillation in Fluids for Active Biodetection,” *Advanced Functional Materials* 35 (2025): 2503213, https://doi.org/10.1002/adfm.202503213.

22. R. Zheng, L. Ma, W. Feng, et al., “Autonomous Self-Sustained Liquid Crystal Actuators Enabling Active Photonic Applications,” *Advanced Functional Materials* 33 (2023): 2301142, https://doi.org/10.1002/adfm.202301142.

23. Z. Hu, Y. Li, and J. A. Lv, “Phototunable Self-Oscillating System Driven by a Self-Winding Fiber Actuator,” *Nature Communications* 12 (2021): 3211, https://doi.org/10.1038/s41467-021-23562-6.

24. V. V. Yashin and A. C. Balazs, “Pattern Formation and Shape Changes in Self-Oscillating Polymer Gels,” *Science* 314 (2006): 798–801, https://doi.org/10.1126/science.1132412.

25. S. Maeda, Y. Hara, T. Sakai, R. Yoshida, and S. Hashimoto, “Self-Walking Gel,” *Advanced Materials* 19 (2007): 3480–3484, https://doi.org/10.1002/adma.200700625.

26. T. Masuda, M. Hidaka, Y. Murase, et al., “Self-Oscillating Polymer Brushes,” *Angewandte Chemie International Edition* 52 (2013): 7468–7471, https://doi.org/10.1002/anie.201301988.

27. A. H. Gelebart, G. Vantomme, E. W. Meijer, and D. J. Broer, “Mastering the Photothermal Effect in Liquid Crystal Networks: A General Approach for Self-Sustained Mechanical Oscillators,” *Advanced Materials* 29 (2017): 1606712, https://doi.org/10.1002/adma.201606712.

28. H. Zeng, M. Lahikainen, L. Liu, et al., “Light-Fuelled Freestyle Self-Oscillators,” *Nature Communications* 10 (2019): 5057, https://doi.org/10.1038/s41467-019-13077-6.

29. G. Vantomme, L. C. M. Elands, A. H. Gelebart, et al., “Coupled Liquid Crystalline Oscillators in Huygens’ synchrony,” *Nature Materials* 20 (2021): 1702–1706, https://doi.org/10.1038/s41563-021-00931-6.

30. T. J. White, N. V. Tabiryan, S. V. Serak, et al., “A High Frequency Photodriven Polymer Oscillator,” *Soft Matter* 4 (2008): 1796–1798, https://doi.org/10.1039/b805434g.

31. S. Serak, N. Tabiryan, R. Vergara, T. J. White, R. A. Vaia, and T. J. Bunning, “Liquid Crystalline Polymer Cantilever Oscillators Fueled by Light,” *Soft Matter* 6 (2010): 779–783, https://doi.org/10.1039/B916831A.

32. K. M. Lee, M. L. Smith, H. Koerner, et al., “Photodriven, Flexural–Torsional Oscillation of Glassy Azobenzene Liquid Crystal Polymer Networks,” *Advanced Functional Materials* 21 (2011): 2913–2918, https://doi.org/10.1002/adfm.201100333.

33. T. Xu, D. Pei, S. Yu, X. Zhang, M. Yi, and C. Li, “Design of MXene Composites With Biomimetic Rapid and Self-Oscillating Actuation Under Ambient Circumstances,” *ACS Applied Materials & Interfaces* 13 (2021): 31978–31985, https://doi.org/10.1021/acsami.1c06343.

34. Q. Wang, Z. Wu, J. Li, J. Wei, J. Guo, and M. Yin, “Spontaneous and Continuous Actuators Driven by Fluctuations in Ambient Humidity for Energy-Harvesting Applications,” *ACS Applied Materials & Interfaces* 14 (2022): 38972–38980, https://doi.org/10.1021/acsami.2c11944.

35. L. Ren, Y. He, B. Wang, et al., “4D Printed Self-Sustained Soft Crawling Machines Fueled by Constant Thermal Field,” *Advanced Functional Materials* 34 (2024): 2400161, https://doi.org/10.1002/adfm.202400161.

36. H. Zhang, H. Zeng, A. Eklund, H. Guo, A. Priimagi, and O. Ikkala, “Feedback-Controlled Hydrogels With Homeostatic Oscillations and Dissipative Signal Transduction,” *Nature Nanotechnology* 17 (2022): 1303–1310, https://doi.org/10.1038/s41565-022-01241-x.

37. Y. Hu, Q. Ji, M. Huang, et al., “Light-Driven Self-Oscillating Actuators With Phototactic Locomotion Based on Black Phosphorus Heterostructure,” *Angewandte Chemie International Edition* 60 (2021): 20511–20517, https://doi.org/10.1002/anie.202108058.

38. S. Hasebe, Y. Hagiwara, T. Goto, et al., “Broad-Wavelength Light-Fueled Organic Crystal Oscillators Driven by Multimodal Photothermally Resonated Natural Vibration,” *Advanced Functional Materials* 34 (2024): 2410671, https://doi.org/10.1002/adfm.202410671.

39. M. Li, Y. Wang, A. Chen, et al., “Flexible Magnetic Composites for Light-Controlled Actuation and Interfaces,” *Proceedings of the National Academy of Sciences* 115 (2018): 8119–8124, https://doi.org/10.1073/pnas.1805832115.

40. C. Jiang, T. Wang, Y. Fu, et al., “All-Protein-Based Rewritable and Reprogrammable Multifunctional Optical Imaging Platforms via Multi-Strategy Imprinting and Multimode 3D Morphing,” *Matter* 7 (2024): 1591–1611.

41. Z. Zhou, S. Zhang, Y. Cao, B. Marelli, X. Xia, and T. H. Tao, “Engineering the Future of Silk Materials Through Advanced Manufacturing,” *Advanced Materials* 30 (2018): 1706983, https://doi.org/10.1002/adma.201706983.

42. B. Peng, X. Chen, G. Yu, et al., “A Neuron-Readable Artificial Photoreceptor Composed of Photodeformable Liquid Crystal Polymers and Piezoelectric Materials,” *Advanced Functional Materials* 33 (2023): 2214172, https://doi.org/10.1002/adfm.202214172.

43. C. R. Bowen, J. Taylor, E. LeBoulbar, D. Zabek, A. Chauhan, and R. Vaish, “Pyroelectric Materials and Devices for Energy Harvesting Applications,” *Energy & Environmental Science* 7 (2014): 3836–3856, https://doi.org/10.1039/C4EE01759E.

44. W. Wei, Z. Zhang, J. Wei, X. Li, and J. Guo, “Phototriggered Selective Actuation and Self-Oscillating in Dual-Phase Liquid Crystal Photonic Actuators,” *Advanced Optical Materials* 6 (2018): 1800131, https://doi.org/10.1002/adom.201800131.

45. D. N. Rockwood, R. C. Preda, T. Yucel, X. Wang, M. L. Lovett, and D. L. Kaplan, “Materials Fabrication From Bombyx mori Silk Fibroin,” *Nature Protocols* 6 (2011): 1612–1631, https://doi.org/10.1038/nprot.2011.379.

Supporting Information

Additional supporting information can be found online in the Supporting Information section.

Supporting File 1: adma72510-sup-0001-SuppMat.docx.
Supplemental File 2: adma72510-sup-0002-MovieS1.mp4.
Supplemental File 3: adma72510-sup-0003-MovieS2.mp4.
Supplemental File 4: adma72510-sup-0004-MovieS3.mp4.
Supplemental File 5: adma72510-sup-0005-MovieS4.mp4.
Supplemental File 6: adma72510-sup-0006-MovieS5.mp4.
Supplemental File 7: adma72510-sup-0007-MovieS6.mp4.
Supplemental File 8: adma72510-sup-0008-MovieS7.mp4.
Supplemental File 9: adma72510-sup-0009-MovieS8.mp4.
Supplemental File 10: adma72510-sup-0010-MovieS9.mp4.
Supplemental File 11: adma72510-sup-0011-MovieS10.mp4.